Coulomb excitation of radioactive ^{21}Na and its stable mirror ^{21}Ne

M. A. Schumaker,[1] D. Cline,[2] G. Hackman,[3] A. C. Morton,[3] C. J. Pearson,[3] C. E. Svensson,[1] C. Y. Wu,[4] A. Andreyev,[3] R. A. E. Austin,[5] G. C. Ball,[3] D. Bandyopadhyay,[1,3] J. A. Becker,[4] A. J. Boston,[6] H. C. Boston,[6] L. Buchmann,[3] R. Churchman,[3] F. Cifarelli,[3] R. J. Cooper,[6] D. S. Cross,[7] D. Dashdorj,[8] G. A. Demand,[1] M. R. Dimmock,[6] T. E. Drake,[9] P. Finlay,[1] A. T. Gallant,[5] P. E. Garrett,[1] K. L. Green,[1] A. N. Grint,[6] G. F. Grinyer,[1,*] L. J. Harkness,[3,6] A. B. Hayes,[2] R. Kanungo,[3,5] K. G. Leach,[1] G. Lee,[3] R. Maharaj,[3] J.-P. Martin,[10] F. Moisan,[11] S. Mythili,[3,12] L. Nelson,[6] O. Newman,[3,13] P. J. Nolan,[6] J. N. Orce,[14] E. Padilla-Rodal,[3] A. A. Phillips,[1] M. Porter-Peden,[15] J. J. Ressler,[7] R. Roy,[11] C. Ruiz,[3] F. Sarazin,[15] D. P. Scraggs,[6] J. C. Waddington,[16] J. M. Wan,[7] A. Whitbeck,[2] S. J. Williams,[3] and J. Wong[1]

[1]*Department of Physics, University of Guelph, Guelph, Ontario N1G 2W1, Canada*
[2]*Department of Physics and Astronomy, University of Rochester, Rochester, New York 14627, USA*
[3]*TRIUMF, 4004 Wesbrook Mall, Vancouver, British Columbia V6T 2A3, Canada*
[4]*Lawrence Livermore National Laboratory, Livermore, California 94551, USA*
[5]*Department of Astronomy and Physics, Saint Mary's University, Halifax, Nova Scotia B3H 3C3, Canada*
[6]*Department of Physics, University of Liverpool, Liverpool, L69 7ZE, United Kingdom*
[7]*Department of Chemistry, Simon Fraser University, Burnaby, British Columbia V5A 1S6, Canada*
[8]*Department of Physics, North Carolina State University, Raleigh, North Carolina 27695, USA*
[9]*Department of Physics, University of Toronto, Toronto, Ontario M5S 1A7, Canada*
[10]*Département de Physique, Université de Montréal, Montréal, Québec H3C 3J7, Canada*
[11]*Département de Physique, Université de Laval, Québec, Québec G1K 7P4, Canada*
[12]*Department of Physics and Astronomy, University of British Columbia, British Columbia V6T 1Z1, Canada*
[13]*Department of Physics, University of Surrey, Guildford, Surrey GU2 7XH, United Kingdom*
[14]*Department of Physics and Astronomy, University of Kentucky, Lexington, Kentucky 40506-0055, USA*
[15]*Physics Department, Colorado School of Mines, Golden, Colorado 80401, USA*
[16]*Department of Physics, McMaster University, Hamilton, Ontario L8S 4L8, Canada*

(Received 2 July 2008; published 23 October 2008)

The low-energy structures of the mirror nuclei ^{21}Ne and radioactive ^{21}Na have been examined by using Coulomb excitation at the TRIUMF-ISAC radioactive ion beam facility. Beams of $\sim 5 \times 10^6$ ions/s were accelerated to 1.7 MeV/A and Coulomb excited in a 0.5 mg/cm^2 $^{\text{nat}}$Ti target. Scattered beam and target particles were detected by the segmented Si detector BAMBINO, while γ rays were observed by using two TIGRESS HPGe clover detectors perpendicular to the beam axis. For each isobar, Coulomb excitation from the $\frac{3}{2}^+$ ground state to the first excited $\frac{5}{2}^+$ state was observed and $B(E2)$ values were determined by using the $2^+ \rightarrow 0^+$ de-excitation in ^{48}Ti as a reference. The ϕ segmentation of BAMBINO was used to deduce tentative assignments for the signs of the mixing ratios between the $E2$ and $M1$ components of the transitions. The resulting $B(E2)\uparrow$ values are $131 \pm 9\, e^2$ fm^4 (25.4 ± 1.7 W.u.) for ^{21}Ne and $205 \pm 14\, e^2$ fm^4 (39.7 ± 2.7 W.u.) for ^{21}Na. The fit to the present data and the known lifetimes determined $E2/M1$ mixing ratios and $B(M1)\downarrow$ values of $\delta = (-)0.0767 \pm 0.0027$ and $0.1274 \pm 0.0025\, \mu_N{}^2$ and $\delta = (+)0.0832 \pm 0.0028$ and $0.1513 \pm 0.0017\, \mu_N{}^2$ for ^{21}Ne and ^{21}Na, respectively (with Krane and Steffen sign convention). By using the effective charges $e_p = 1.5e$ and $e_n = 0.5e$, the $B(E2)$ values produced by the p-sd shell model are 30.7 and 36.4 W.u. for ^{21}Ne and ^{21}Na, respectively. This analysis resolves a significant discrepancy between a previous experimental result for ^{21}Na and shell-model calculations.

DOI: 10.1103/PhysRevC.78.044321 PACS number(s): 25.70.De, 26.30.Ca, 27.30.+t, 29.30.Kv

I. INTRODUCTION

The nucleus ^{21}Na occupies a vital position in the rapid proton-capture process (rp-process), as the dominant breakout pathways from the hot carbon-nitrogen-oxygen (hCNO) cycle into the rp-process proceed through this radioactive isotope of Na. This process occurs at the extreme temperature and pressure conditions of $T \leqslant 2.1$ GK and $\rho \leqslant 10^7$ g/cm^3 [1] found in the accretion layers of neutron stars in binary star systems. The ^{18}Ne$(\alpha, p)^{21}$Na [2–4] reaction leads directly to this nucleus, whereas at lower temperatures [5] the flow proceeds from ^{19}Ne via ^{19}Ne$(p,\gamma)^{20}$Na$(p,\gamma)^{21}$Mg$(\beta^+\nu)^{21}$Na. These pathways combine, along with possible contributions from ^{17}F$(\alpha,\gamma)^{21}$Na and ^{20}Na$(\beta^+\nu)^{20}$Ne$(p,\gamma)^{21}$Na, to outflow through ^{21}Na$(p,\gamma)^{22}$Mg [6,7] or ^{21}Na$(\beta^+\nu)^{21}$Ne, making ^{21}Na a key link from the hCNO cycle through the NeNa region and beyond [6].

Although the level structure of ^{21}Na below the proton-separation energy has been determined through in-beam γ-ray spectroscopy [8], information concerning transition matrix elements, a more sensitive probe of nuclear structure, is very limited for ^{21}Na. The decay lifetimes of the first two excited states, $\frac{5}{2}^+$, 331.9 keV and $\frac{7}{2}^+$, 1716.1 keV are dominated by $M1$ transitions, and the $B(M1)$ values are

[*]Present address: National Superconducting Cyclotron Laboratory, Michigan State University, East Lansing, Michigan 48824, USA.

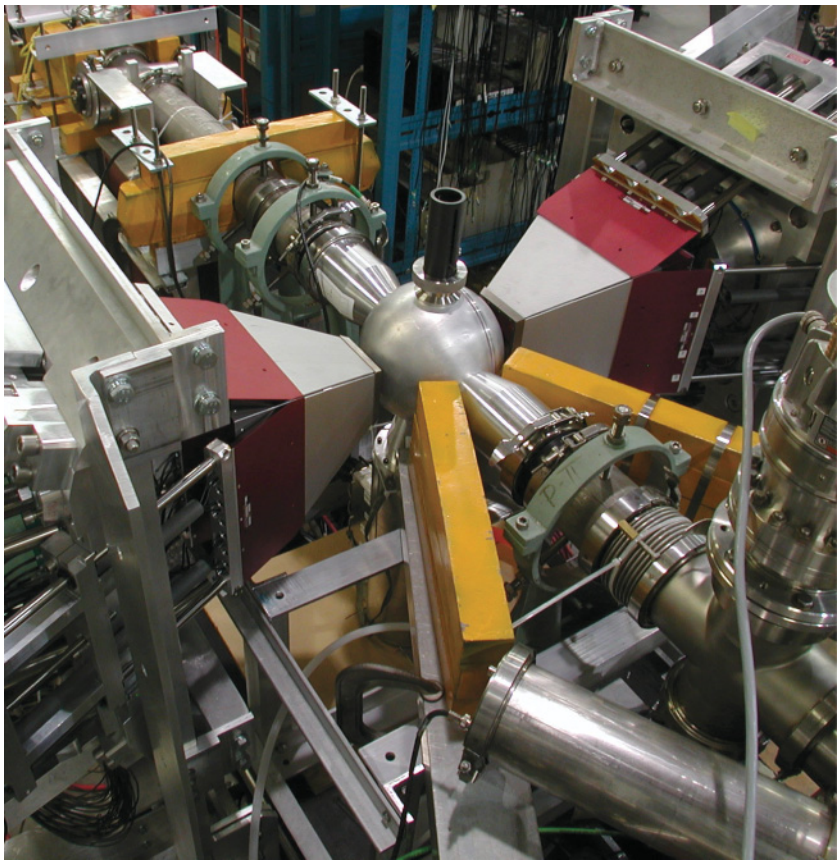

FIG. 1. (Color online) Two TIGRESS HPGe clover detectors perpendicular to the beam axis with their BGO + CsI Compton-suppression shields mounted to either side of the BAMBINO target chamber at the TRIUMF-ISAC facility.

well determined by previous lifetime measurements [8–11]. However, the uncertainties in the mixing ratio for the $\frac{5}{2}^+$ excited state decay and the branching ratio for the $\frac{7}{2}^+$ excited state decay [12] lead to highly uncertain $B(E2)$ values of $B(E2; \frac{3}{2}^+ \rightarrow \frac{5}{2}^+) = 14 \pm 12$ W.u.[1] and $B(E2; \frac{3}{2}^+ \rightarrow \frac{7}{2}^+) = 16 \pm 8$ W.u. for these transitions. Only one other transition has matrix elements quoted in Ref. [8], the decay of the second $\frac{5}{2}^+$ state at 3544 keV to the ground state. It is unclear, however, whether the analysis of the decay of this level [13] took into account its location above the proton separation energy, since it has been shown that decay from this level is nearly 100% by proton emission to states in ^{20}Ne [3] and the $B(M1)$ and $B(E2)$ values quoted differ by almost two orders of magnitude from shell-model calculations [14]. The accuracy of the $B(E2; \frac{3}{2}^+ \rightarrow \frac{5}{2}^+)$ value in ^{21}Na is also questionable. In comparing the mirror pair, the values of 24 ± 3 W.u. for ^{21}Ne and 14 ± 12 W.u. for ^{21}Na are difficult to understand as shell-model calculations in this region universally predict a larger $B(E2; \frac{3}{2}^+ \rightarrow \frac{5}{2}^+)$ for the more proton-rich ^{21}Na.

In the present work, precise $B(E2; \frac{3}{2}^+ \rightarrow \frac{5}{2}^+)$ values are established for both radioactive ^{21}Na and stable ^{21}Ne through direct Coulomb excitation of accelerated beams of these isobars, and the discrepancy of the previous ^{21}Na data with shell-model predictions is resolved.

[1]A typographical error in Ref. [8]a incorrectly listed this as 40 ± 3 W.u. The value given here is based on the mixing ratio in Ref. [12], as corrected on the National Nuclear Data Center (NNDC) Web site.

II. EXPERIMENT

The experiment described here was the first to use detectors of the TRIUMF-ISAC Gamma-Ray Escape-Suppressed Spectrometer (TIGRESS) [15–20], a high-efficiency γ-ray detector array designed for use with the accelerated radioactive ion beams (RIBs) available at the ISAC facility at TRIUMF [21]. The four HPGe crystals per TIGRESS clover detector module are electrically segmented to allow better γ-ray interaction location determination for improved Doppler correction. The eight segments per crystal are created by two longitudinal segmentations and one lateral one. The position sensitivity will be enhanced by using analysis of the resulting waveforms [15]. For this experiment, two TIGRESS HPGe clover detectors were aligned perpendicular to the beam axis around a target vacuum chamber, as shown in Fig. 1. In conjunction with the TIGRESS detectors, the BAMBINO segmented Si CD detector was used for particle detection. BAMBINO consists of 24 θ-slice rings, spanning laboratory angles from 20.1° to 49.4° relative to the beam axis, and 14 active ϕ-slice sectors, each covering a ϕ range of 22.5°. The high efficiency of the TIGRESS detectors, when used in combination with auxiliary particle detection systems such as BAMBINO, makes TIGRESS a highly sensitive instrument for experiments with RIBs [22]. After preamplification, detector waveforms were processed by using the custom-designed TIG-10 and TIG-C digital electronics modules, which provided 100-MHz, 14-bit continuous waveform digitization of preamplifier signals from the HPGe, Compton-suppression shield, and Si detectors [23].

To access directly the low-energy transition matrix elements in ^{21}Ne and ^{21}Na, Coulomb excitation was used. The preferential selection of the $E2$ excitation component to the first excited state was important for this study, owing to the dominance of the $M1$ component in the decay. Production of ^{21}Ne was accomplished by using the Off-Line Ion Source (OLIS) at ISAC, and isotopically pure ^{21}Na was produced by using proton-induced fragmentation of a Ta target, with surface ionization and charge-to-mass separation. In this experiment, beams of $\sim 5 \times 10^6$ ions/s were used, which was the limit imposed by the full waveform readout from all TIG-10 electronics modules for every event in this first experiment, rather than beam availability [24].

For each beam, the ions were accelerated to 1.700 MeV/A using the ISAC-I radio-frequency quadrupole and drift-tube linear accelerators [21] and directed toward a thin target of ^{nat}Ti at the center of the TIGRESS target chamber. Ti was chosen to take advantage of the 983.5-keV $2^+ \rightarrow 0^+$ de-excitation γ ray from ^{48}Ti, for which the $B(E2)$ value is well known [25], to normalize the γ-ray yields from the beam particle de-excitation. The target thickness was determined to be 0.5 mg/cm^2 by direct mass and area measurement and by the comparison of energy-loss measurements of the α particles from ^{239}Pu, ^{241}Am, and ^{244}Cm to SRIM [26] calculations. The BAMBINO CD detector was located 3.0 cm downstream of the target and was used to detect both scattered projectile particles and forward-recoiling target particles. The segmentation of BAMBINO was used to separate the particle-coincident data into angular bins and to assist in Doppler correction of the γ-ray energies. This segmentation, as well as the high segmentation of the TIGRESS detectors, provided excellent Doppler correction, resulting in well-defined γ-ray photopeaks, as shown in Sec. IV.

III. ANALYSIS

A. Determination of γ-ray yields

The full particle-γ coincidence data were separated into multiple spectra, based on particle scattering angle. For the Si detector, a coincidence between a hit in a θ ring and a hit in a ϕ sector was required. This was based on the application of a time-difference acceptance gate. A low-energy threshold was also introduced to the Si energies to eliminate detections of recoiling ^{12}C, which resulted from a buildup of beamline contaminant. This contaminant also led to beam particle detection after scattering from ^{12}C, so the innermost ring was omitted from analysis. Particle energy gates were also applied to the Si ring energy spectra to separate Ti target particle detection from beam particle detection. These particles occupied distinct energy ranges in the spectra, as shown in Fig. 2 for the 21.8° to 23.4° ring (upper) and 40.9° to 42.0° BAMBINO ring (lower). Hits to multiple sectors or nonadjacent rings were excluded from analysis, but the energy depositions from hits to adjacent rings were summed and compared against the particle energy gates. Particle-γ coincidences recovered this way were attributed to the lower angle ring of the adjacent pair. The small gap between the rings in which these events take place results in relatively few of these counts. To determine the scattering angle of recoiling target particles in the case of beam particle detection, or scattered beam particles in the case of target particle detection, kinematic calculations were performed that included the effects of particle energy loss through the target material both before and after the scattering event. The location of the scattering event was assumed to be the center of the target, and energy losses were determined by interpolation using parametrized fits to SRIM [26] output.

The energy loss of the recoiling Ti particles through the target was such that at higher forward (Ti detection) recoil angles, 42.0° to the outer edge at 49.4°, the Ti energy distribution fell below the low-energy cutoff mentioned previously, making it impossible to determine the number of counts accurately. Ti particle detection was not analyzed for these rings. In addition, for a range of Ti particle detection angles, the rings corresponding to 28.1° to 36.3°, the corresponding beam particle scattering angles were approximately perpendicular to the beam axis (81.7° to 98.1°). These particles stopped inside the target, resulting in γ-ray emissions from inside the Ti. The result was a decrease in the coincident γ-ray yields owing to scattering within the Ti target and the target frame, and events in these rings were therefore removed from consideration when determining coincident yields for beam particle excitation, though not when considering excitation of ^{48}Ti.

Twelve sectors were used for particle coincidences. By taking $\phi = 0°$ to be vertical relative to the beam axis, the two (22.5° each) sectors neighboring 180° were inactive by design to accommodate the electronic readouts. The two sectors neighboring 0° were also excluded from analysis because of acquisition problems. The determination of particle-γ coincidences was accomplished with the application of a time-difference acceptance gate between Si rings and HPGe detector events. Compton-scattered γ-ray events were suppressed by using the full TIGRESS BGO + CsI Compton-suppression shield [16] during offline analysis, and add-back of energy depositions in multiple crystals was used to recover additional full-energy events [18]. Two Doppler corrections were applied to the γ rays, based on the assumption of beam particle excitation or ^{48}Ti excitation. This created separate γ-ray spectra with which to determine the yields of γ rays from either reaction partner (Figs. 3 and 4). Particle-γ coincident events were sorted as a function of angles defined by sets of rings and sectors. The peak areas in the coincident γ-ray spectra were determined for analysis. The particle-γ coincident yields separated by sectors (ϕ distributed) were divided into sector pairs covering 45°, and the particle-γ coincident yields separated by rings (θ distributed) were divided into the regions described in Tables I and II for beam projectile and target particle excitation, respectively. To reduce the number of random particle-γ coincidences, a time-random subtraction was applied. Gates placed on the time-difference values not in the coincidence peak were used to create time-random spectra, which were subtracted from the full particle-γ coincidence spectra shown in Figs. 3 and 4.

Peaks in the resulting γ spectra were fit to determine peak areas. These were corrected for γ-ray relative efficiency by using data from ^{133}Ba and ^{152}Eu calibration sources. The difference in the absolute efficiencies of the two TIGRESS detectors was examined by using a ^{60}Co source, and the results

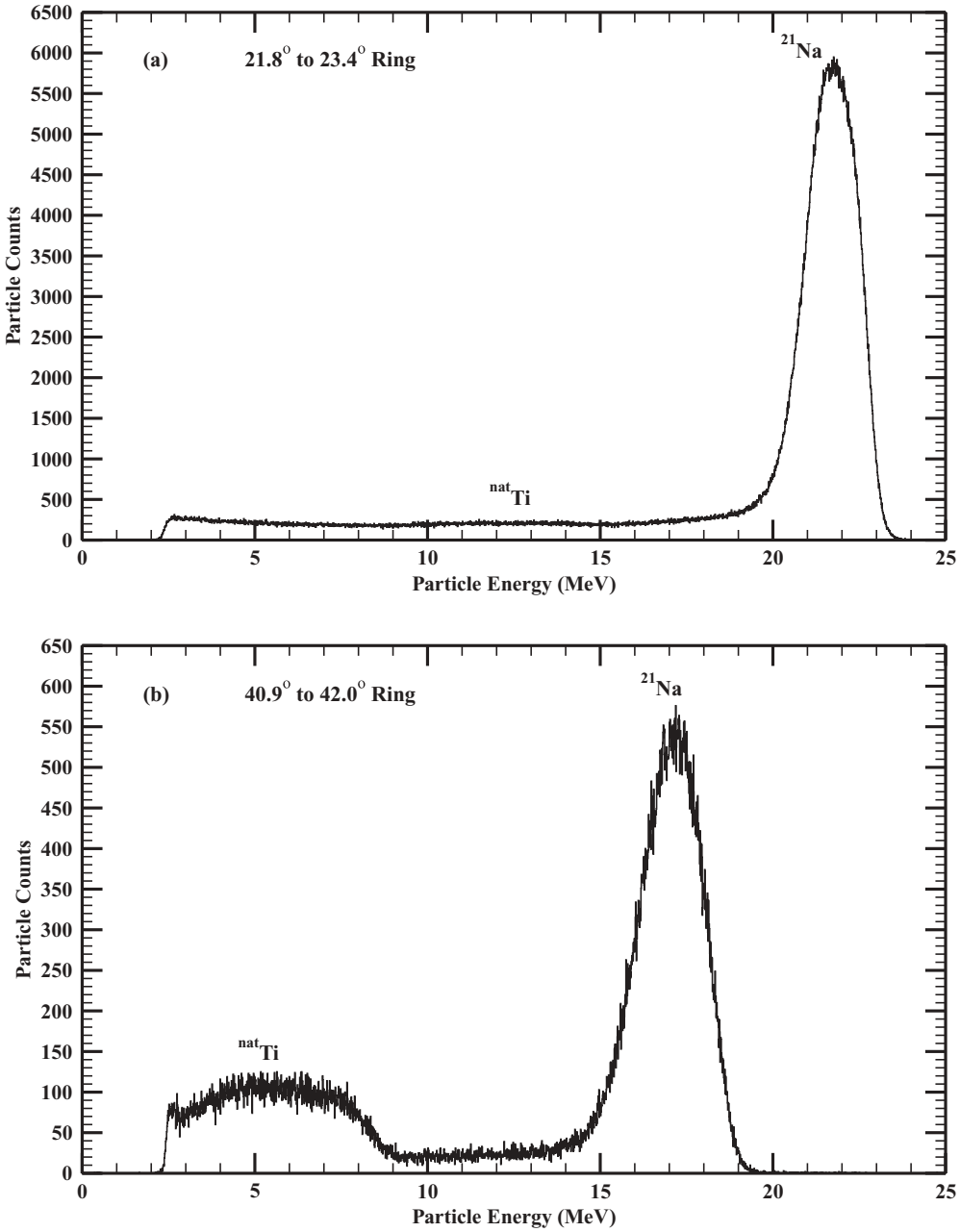

FIG. 2. Particle energies deposited in BAMBINO rings for the ring covering (a) 21.8° to 23.4° and for the ring covering (b) 40.9° to 42.0°. The separate energy depositions from the ^{21}Na particles and Ti particles are identified.

from one detector (identified as Detector 2 in the results) were corrected by the 0.918(11) ratio of the absolute efficiencies to account for this difference.

A correction was also applied to the ϕ-distributed yields. It was determined that the beam spot location was not perfectly centered with respect to the central axis of the BAMBINO Si CD. For the ^{21}Ne data, the beam spot center was below the center of BAMBINO, whereas for the ^{21}Na data the beam spot center was above. The offset was quantified by comparing pairs of sector particle counts above and below the horizontal axis, in relation to an offset of the Rutherford scattering cross section. Through this analysis it was determined that for the ^{21}Ne data the beam location was under the CD center by 0.20 mm, whereas for the ^{21}Na data the beam spot was above the CD center by 0.67 mm. These offsets were significantly smaller than the beam spot diameter of ∼3 mm, but still produced an observable change that required correction. The sector yields were fit to the function counts $= A \sin(\phi + B) + C$ and the resulting function was divided by the average counts. The resulting "sector correction factor" function is plotted in Fig. 5 for ^{21}Ne (a) and ^{21}Na (b), with the counts from the BAMBINO sectors to which they were fit. Uncertainties in the sector particle counts were taken to be the square root of the counts. The uncertainties in the fit function parameters were negligible, with relative values of 0.06% for parameter C (the average) and less than 0.3% for parameter A (the magnitude of the

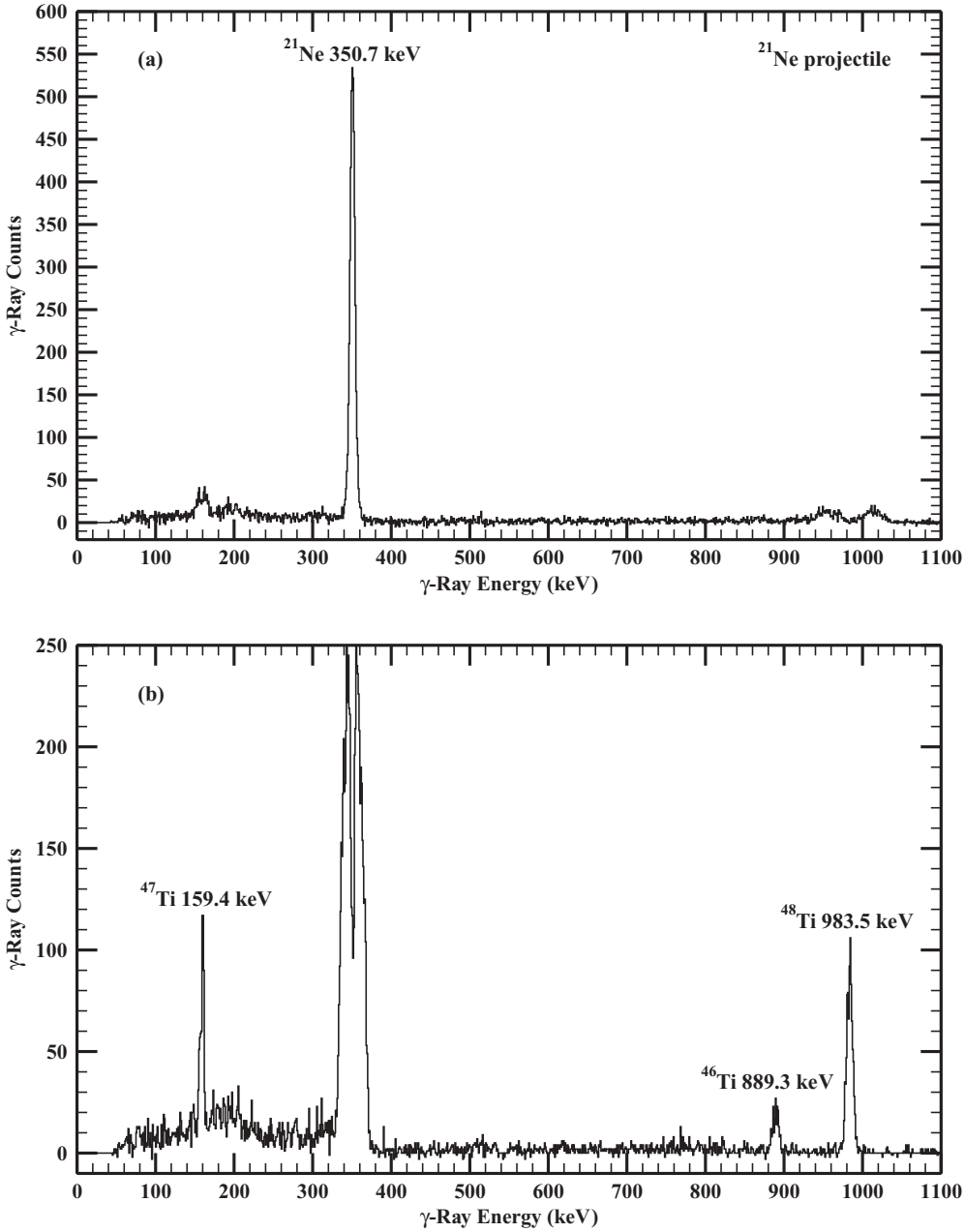

FIG. 3. Gamma-ray spectrum of all data utilized for the ^{21}Ne beam, Doppler corrected by assuming (a) ^{21}Ne excitation or (b) ^{48}Ti excitation.

sine variation) and an uncertainty of parameter B significantly smaller than the sector size. The variation in the fit function owing to the uncertainty in parameter A is shown in Fig. 5.

Particle-γ coincident yields were divided by these sector correction factors to normalize them to the scattered particle distribution. The resulting yields were compared to calculations of expected Coulomb excitation yields to obtain the final results.

B. GOSIA calculations

Calculations to determine matrix-element-dependent γ-ray yields were performed by using GOSIA [27]. For the beam particles, matrix elements and branching ratios were included for transitions and static moments involving the $\frac{3}{2}^+$ ground state and the first excited $\frac{5}{2}^+$, $\frac{7}{2}^+$, and $\frac{9}{2}^+$ levels. For ^{48}Ti, the 0^+ ground state, first and second excited 2^+, first and second 4^+, and first 6^+ levels were considered.

Known lifetimes, mixing ratios, and branching ratios from Refs. [8,9,25,28–32] were used as input values for the calculations. For matrix elements in ^{48}Ti involving states above the first 2^+, for which information was limited, the quadrupole rotor model values were used. For the beam particles, transitions for which experimental data did not exist or were imprecise were taken from p-sd shell-model calculations [33,34], which considered nucleon interactions within the $1p_{1/2}$ and sd shell space around an inert ^{12}C core. The uncertainty contributions from all of these parameters are

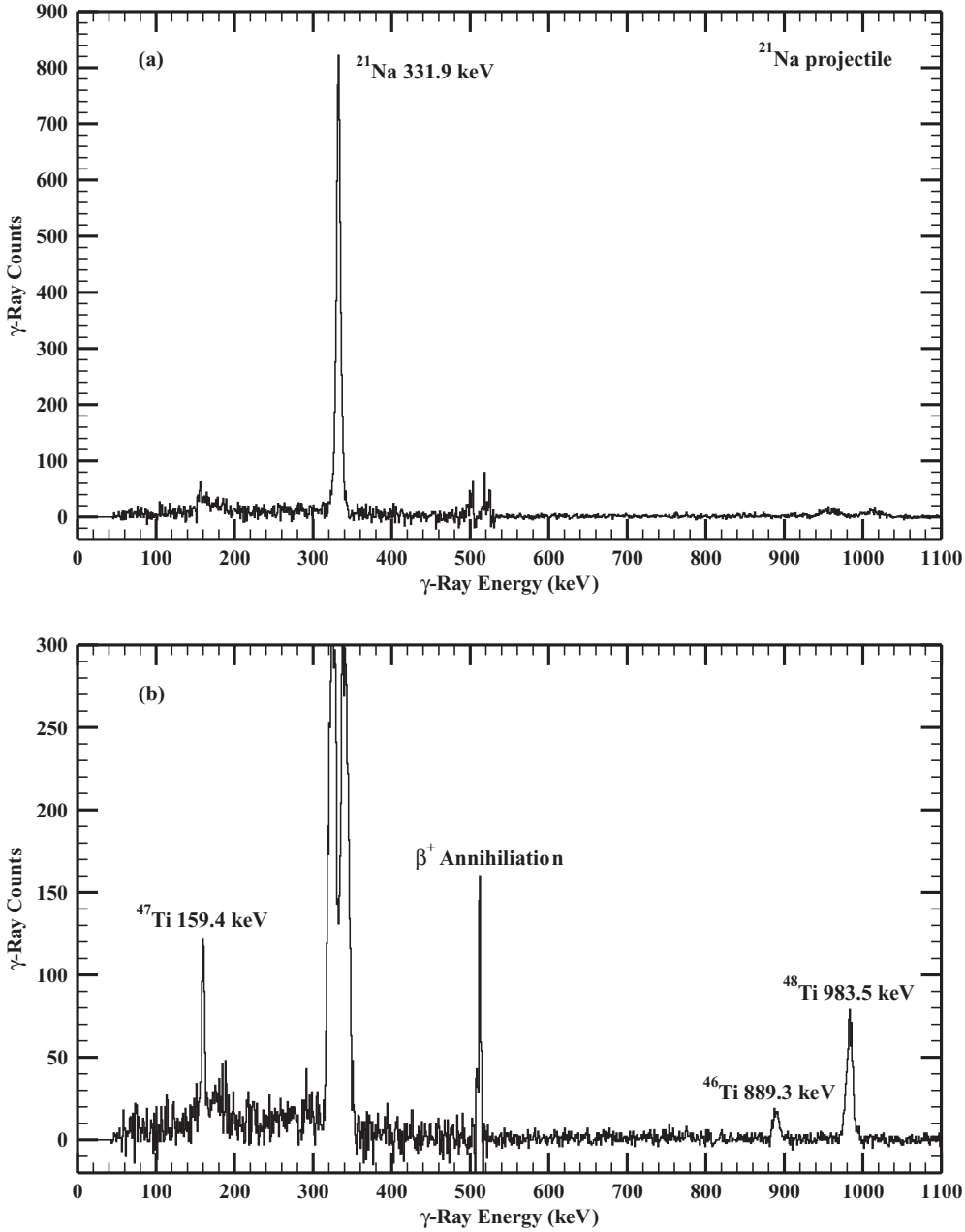

FIG. 4. Same as in Fig. 3, but for the ^{21}Na radioactive beam.

TABLE I. The angular regions over which particle detection was taken in coincidence with γ-ray detections at the energy of the first excited state of the beam projectile particle. All angles are given in the laboratory frame.

Detected angles	Particle	Projectile angles	Target angles
21.8°–29.5°	Projectile	–	74.4°–69.0°
29.5°–37.5°	Projectile	–	69.0°–63.5°
37.5°–44.0°	Projectile	–	63.5°–59.1°
44.0°–49.4°	Projectile	–	59.1°–55.6°
42.0°–35.0°	Target	73.4°–84.2°	–
28.1°–21.8°	Target	98.1°–112.6°	–

TABLE II. The angular regions over which particle detection was taken in coincidence with γ-ray detections at the energy of the first excited state of ^{48}Ti. All angles are given in the laboratory frame.

Detected angles	Particle	Projectile angles	Target angles
21.8°–29.5°	Target	112.6°–95.2°	–
29.5°–36.3°	Target	95.2°–81.7°	–
36.3°–42.0°	Target	81.7°–71.5°	–
49.4°–44.0°	Projectile	–	55.6°–59.1°
44.0°–37.5°	Projectile	–	59.1°–63.5°
37.5°–29.5°	Projectile	–	63.5°–69.0°
29.5°–21.8°	Projectile	–	69.0°–74.4°

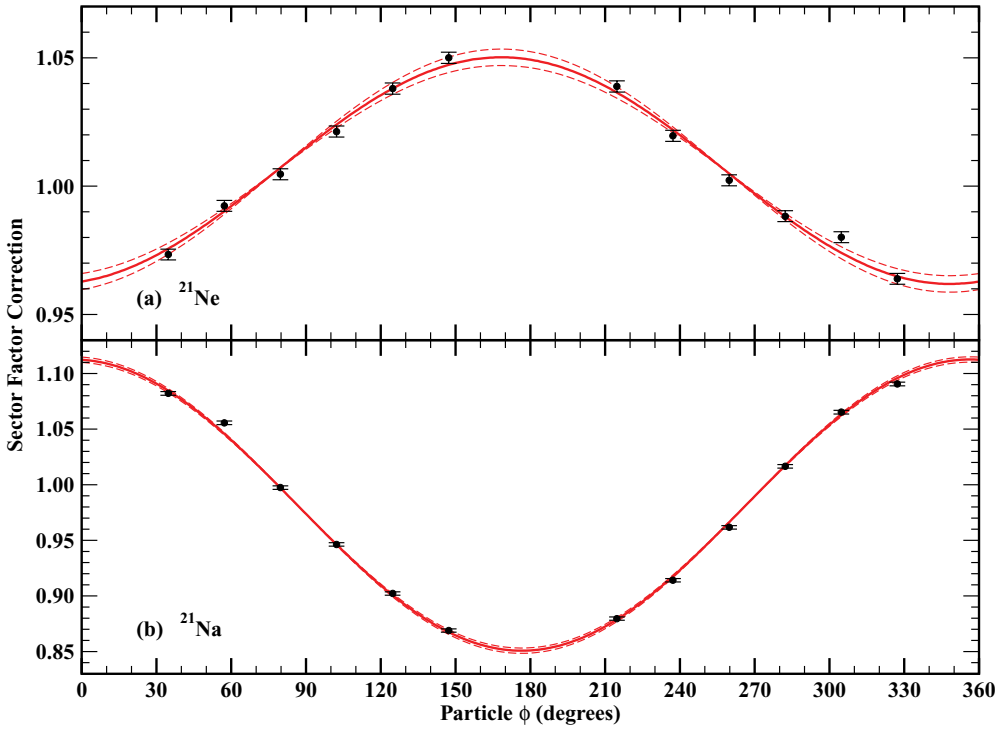

FIG. 5. (Color online) Determination of the sector correction factors based on fits to the ϕ-distributed particle detection yields, resulting from the offset of the beam location from the target center. Sector yields are shown with error bars; the fit function and the uncertainty from parameter A (the magnitude of the sine function variation about the average) are shown as solid and dashed lines, respectively.

discussed in Sec. IV B. The energy loss of the beam particles passing through the target was calculated by using SRIM [26].

GOSIA requires input of the angular attenuation factors (Q) to account for the finite solid angle of the γ-ray detectors. GOSIA assumes the detectors have cylindrical symmetry, allowing the use of simple attenuation factors that ignore ϕ dependence. These attenuation factors are expressed as [35]

$$Q_k(E_\gamma) = \frac{J_k(E_\gamma)}{J_0(E_\gamma)}, \tag{1}$$

where

$$J_k(E_\gamma) = \int_0^{\alpha_{\max}} P_k(\cos\alpha)[\epsilon_{\rm abs}(\alpha, E_\gamma)] \sin\alpha \, d\alpha, \tag{2}$$

E_γ is the γ-ray energy, α is the angle from the central axis of the HPGe detector, P_k are the Legendre polynomials, and $\epsilon_{\rm abs}$ is the γ-ray energy- and angle-dependent absolute photopeak efficiency. The TIGRESS HPGe clovers do not have cylindrical symmetry, and so an accurate GEANT4 [36] simulation of the TIGRESS detectors [18] was used to determine $\epsilon_{\rm abs}$ for the full range of relevant angles and γ-ray energies up to 2 MeV. For each set of conditions, $\epsilon_{\rm abs}$ was determined by Monte Carlo techniques by simulating the random paths of a large set of γ rays. For each γ-ray energy, numerical integration was performed over the angle α by summing contributions from the angles simulated. To accommodate the ϕ asymmetry, the ϕ emission angle was randomized to provide an average for each angle α. To provide an accurate model of the variations in efficiency with α angle, GOSIA uses contributions from attenuation factors with $k = 1$ to $k = 8$. For each, the required input is reduced to three values by parametrizing the γ-ray energy dependence, using the fit function

$$Q_k(E_\gamma) = \frac{C_2 Q_k(E_0) + C_1(E_\gamma - E_0)^2}{C_2 + (E_\gamma - E_0)^2}, \tag{3}$$

where E_0 is a lower cutoff energy, set to be 50 keV. For each value of k, Q_k(50 keV) and the fit parameter results C_1 and C_2 were used as input to GOSIA to describe the TIGRESS detectors. The effect of this modification is discussed in Sec. IV B1.

IV. RESULTS

Coulomb excitation from the $\frac{3}{2}^+$ ground state to the $\frac{5}{2}^+$ first excited state was observed for both ^{21}Ne and ^{21}Na. The de-excitation γ rays from the $2^+ \rightarrow 0^+$ transition in ^{48}Ti were also detected, providing reference yields with which to determine $B(E2)$ values for the beam particles. As shown in Figs. 3 and 4, the peak-to-total ratios for the beam excitation γ rays were excellent and the uncertainties on the number of counts in the peaks of interest had a negligible dependence on the time-random subtraction. For both nuclei, the fraction of the uncertainty resulting from the time-random subtraction in the θ-dependent particle-γ yields was less than 0.6%. For ^{48}Ti excitation, owing to the lower number of counts, the subtraction introduced a larger proportion of the uncertainty, though this remained less than 2.9% of the uncertainty for the ^{21}Ne experiment and less than 8.0% for the ^{21}Na experiment

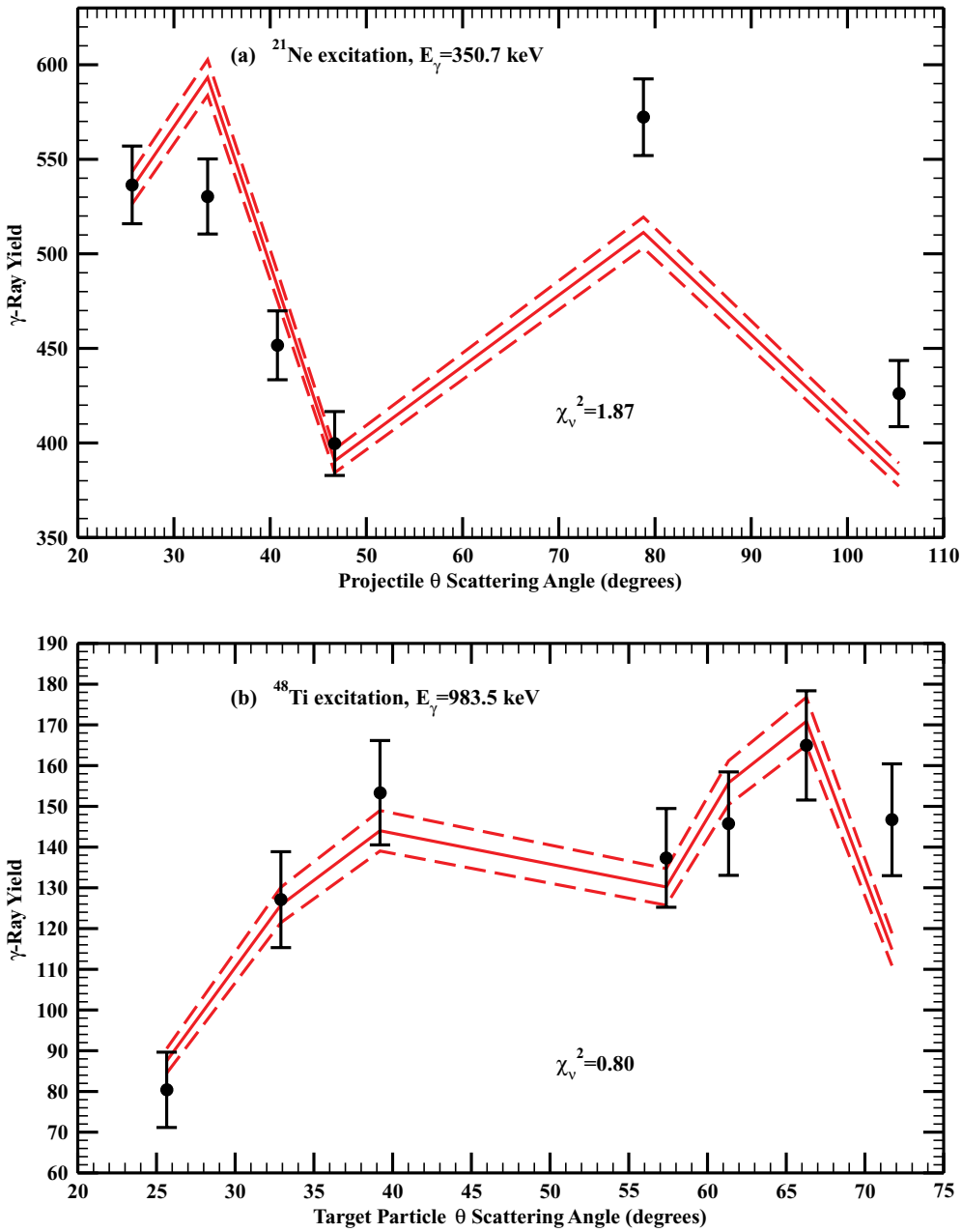

FIG. 6. (Color online) Fit results of GOSIA to the experimental yields used to determine $B(E2)$ to the first excited state of ^{21}Ne.

for the innermost sets of rings, and less than 1% when averaged over all particle-γ θ regions.

A. Fits to experimental data

$B(E2)$ values relative to ^{48}Ti $B(E2; 0^+ \rightarrow 2^+)$ were determined by the normalization factors between GOSIA and the experimental yields. Taking a ratio of these normalization factors, incorporating the abundance of ^{48}Ti in $^{\text{nat}}$Ti (73.72%), and applying the resulting quotient to the known $E2$ transition matrix element for the excitation in ^{48}Ti provided absolute $E2$ transition matrix elements for the beam particles. The value of the $E2$ transition matrix element used in the GOSIA calculations was iterated until convergence was achieved. For each isobar, adjustment was then made to the input value of the $M1$ matrix element to match the known lifetime for a final iteration. The resulting GOSIA fits to the experimental data are shown in Figs. 6 and 7 for ^{21}Ne and ^{21}Na, respectively. $B(E2)\downarrow$ values of 87.5 ± 3.6 and $136.5 \pm 6.0\, e^2$ fm^4 were obtained for ^{21}Ne and ^{21}Na, respectively. These uncertainties are statistical and include inflation by $\sqrt{\chi_\nu^2}$ for those fits with $\chi_\nu^2 > 1$. Further uncertainty contributions will be discussed in Sec. IV B.

These fits used mixing ratio signs as described for these nuclei in Ref. [8]. By using fits to the data divided among sector angle slices to examine the ϕ distribution, the possibility of determining these signs was explored. By using the phase convention of Ref. [37], the adopted signs are negative for

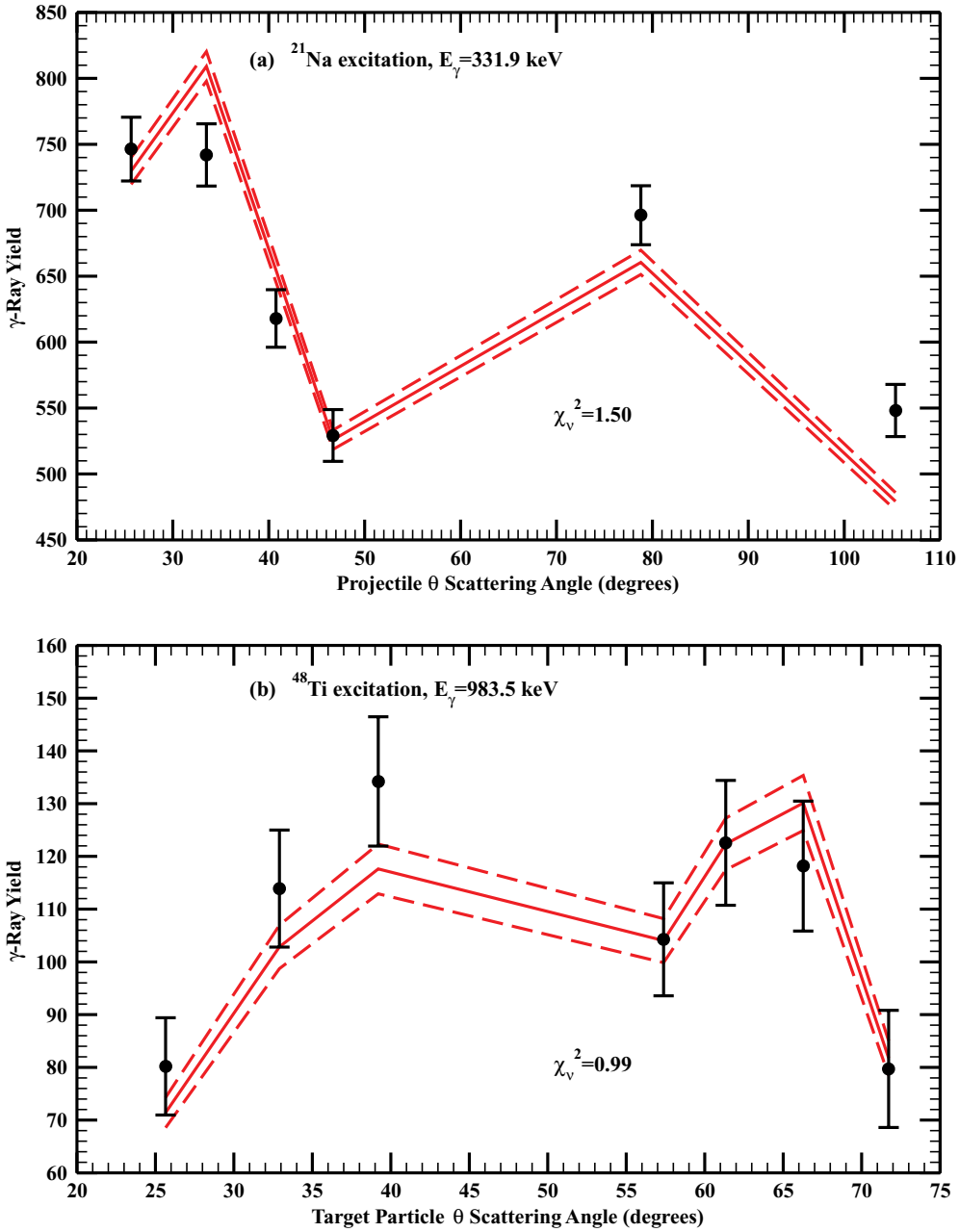

FIG. 7. (Color online) Same as in Fig. 6, but for the ^{21}Na radioactive beam.

^{21}Ne and positive for ^{21}Na. These were tested by examining fits of GOSIA output with the assumption of both mixing ratios and examining the resulting differences in the quality of the fits. Three θ ranges were examined for each set of ϕ angles: projectile particle detection from 21.8° to 49.4° and target particle detection from 21.8° to 28.1° and 36.3° to 42.0°. The results of these fits are shown in Fig. 8. As stated previously, data were separated among γ-ray detectors.

The resulting χ_ν^2 values (using one free parameter) are $\chi_{\nu+}^2 = 1.90$ and $\chi_{\nu-}^2 = 1.59$ for ^{21}Ne and, $\chi_{\nu-}^2 = 1.85$ and $\chi_{\nu+}^2 = 1.72$ for ^{21}Na. These indicate that the optimal sign assignments from this work are consistent with those previously assigned. With the use of a statistical F-test, the significance of the difference in these χ_ν^2 values was tested, and in both cases it was found to be insufficient to reject the possibility of the opposite signs. As a result, only tentative confirmations of a negative mixing ratio for ^{21}Ne and a positive mixing ratio for ^{21}Na are made.

B. Uncertainty contributions

In addition to the statistical uncertainties in the $B(E2)\downarrow$ values from the fits (±3.6 and ±6.0 e^2 fm^4 for ^{21}Ne and ^{21}Na, respectively), a number of other uncertainty contributions were considered. The first of these is the uncertainty in the matrix element for the first transition in ^{48}Ti ($B(E2; 2^+ \rightarrow 0^+)\downarrow = 152.2 \pm 3.8\, e^2$ fm^4 [25]), since it serves as the normalization reference in this experiment. This contributes uncertainties of

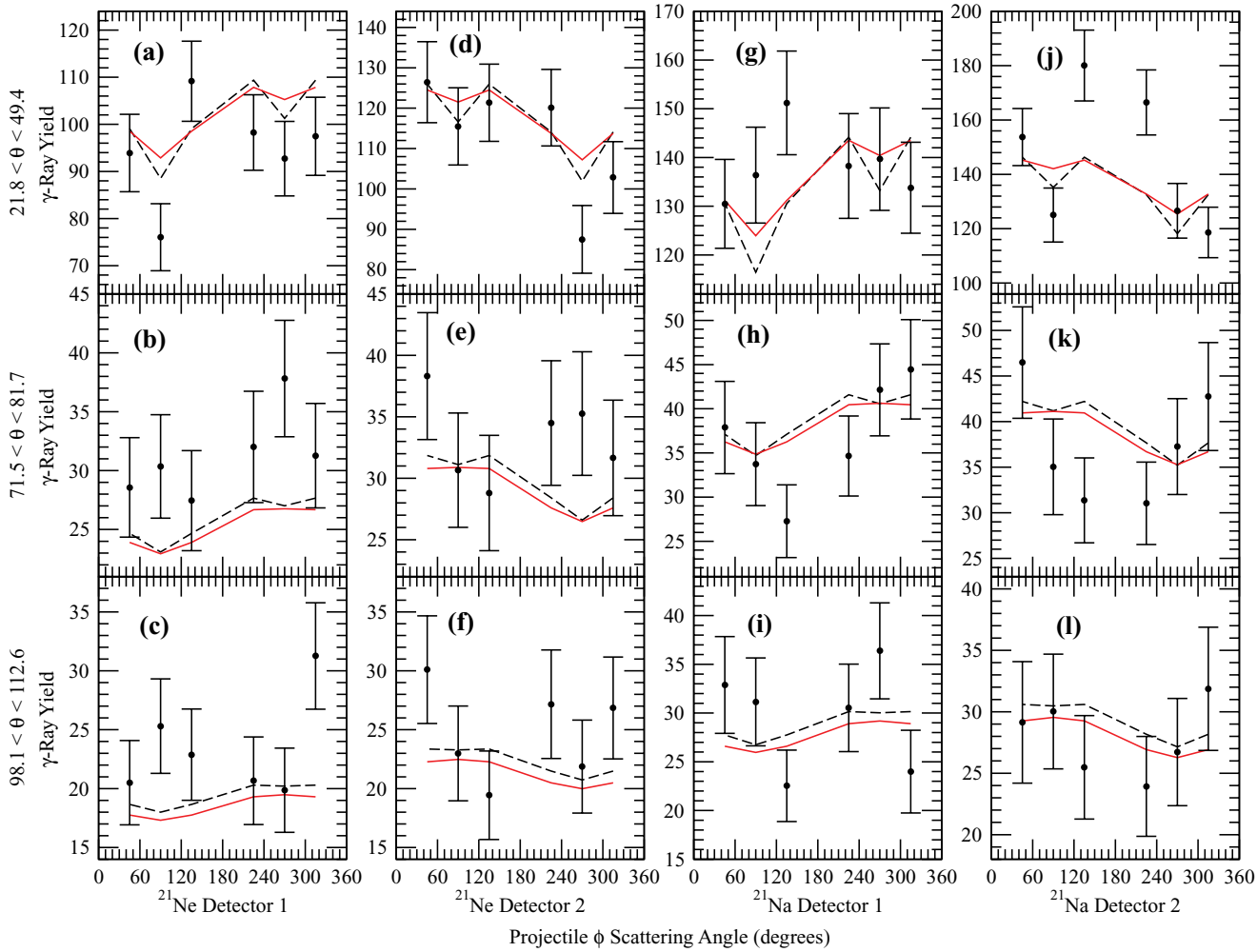

FIG. 8. (Color online) Yields as a function of ϕ angle for three θ regions, for ^{21}Ne (left-most and center-left columns) and ^{21}Na (center-right and right-most columns). Figures 8(a), 8(d), 8(g), and 8(j) show the ϕ results for projectile angles $21.8^\circ \leqslant \theta \leqslant 49.4^\circ$; Figs. 8(b), 8(e), 8(h), and 8(k) correspond to projectile angles $71.5^\circ \leqslant \theta \leqslant 81.7^\circ$; and Figs. 8(c), 8(f), 8(i), and 8(l) correspond to projectile angles $98.1^\circ \leqslant \theta \leqslant 112.6^\circ$. Experimental yields are shown in black with error bars, the results of GOSIA calculations using negative mixing ratios are shown with dashed black lines, and the results of calculations using positive mixing ratios are shown with solid red lines.

± 1.6 and $\pm 2.5\, e^2$ fm^4 for ^{21}Ne and ^{21}Na, respectively. Each additional uncertainty is discussed in the following, and all are summarized in Table III.

1. Detector model

The procedure by which the γ-ray energy attenuation factors were determined was described in Sec. III B. To determine the sensitivity of the results to this model, the GOSIA calculations were repeated by using a simplified model of the detector generated by GOSIA, which approximated a TIGRESS detector as a simple cylinder of similar size to the TIGRESS HPGe clover. This resulted in slight deviations of only ± 0.19 and $\pm 0.21\, e^2$ fm^4 for ^{21}Ne and ^{21}Na, respectively.

2. Assumed mixing ratio sign

Since our data are inconclusive with regard to the mixing ratio signs, the GOSIA calculations were performed with the opposite sign to determine the resulting sensitivity of the $B(E2)$ values. The uncertainties related to this variation are ± 0.77 and $\pm 1.5\, e^2$ fm^4 for ^{21}Ne and ^{21}Na, respectively.

3. Initial beam energy

The precise tuning of the ISAC beam energy [21] resulted in a small uncertainty in the initial beam energy of 1.700 ± 0.003 MeV/A. The effect of using the upper and lower limits of this beam energy was explored in the GOSIA calculations. The uncertainties related to this variation are ± 0.54 and $\pm 1.0\, e^2$ fm^4 for ^{21}Ne and ^{21}Na, respectively.

4. Target thickness

As discussed in Sec. II, the target thickness was determined both by direct mass and area measurement and by a comparison between the measured energy loss of α particles through the $^{\text{nat}}$Ti and SRIM [26] calculations. The uncertainty in this procedure was taken to be $\sim$10%. This uncertainty was

TABLE III. Contributions to the uncertainties in the $B(E2)\downarrow$ values in e^2 fm^4. The quadrature sum was determined by using the larger magnitude when the upper and lower limits differed.

Effect	^{21}Ne	^{21}Na
Statistical error	±3.6	±6.0
^{48}Ti $0^+ \rightarrow 2^+$	±1.6	±2.5
Detector model	±0.19	±0.21
Assumed mixing ratio sign	±0.77	±1.5
Initial beam energy 1.700 ± 0.003 MeV/A	±0.54	±1.0
Target thickness $\pm10\%$	$^{+1.6}_{-1.3}$	$^{+3.1}_{-2.8}$
^{48}Ti 2^+ quadrupole moment	$^{+2.8}_{-1.0}$	$^{+4.0}_{-1.4}$
$\frac{5}{2}^+$ quadrupole moment	$^{+0.27}_{-0.05}$	$^{+0.9}_{-0.2}$
$\frac{3}{2}^+ \rightarrow \frac{7}{2}^+$ $E2$ matrix element	$^{+0.02}_{-0.01}$	-0.66
Other ^{48}Ti matrix elements	$^{+0.53}_{-0.36}$	$^{+0.71}_{-0.36}$
Other ^{21}Ne, ^{21}Na elements	$^{+0.74}_{-0.21}$	$^{+1.1}_{-0.4}$
Rutherford orbit corrections	±0.4	±0.7
Nuclear and quantal corrections	±2.4	±3.3
Quadrature sum	$\pm$**5.8**	$\pm$**9.2**

used to find new final energies, integration mesh points, and stopping powers from SRIM for use in the GOSIA calculations. The variation in the $B(E2)\downarrow$ values that resulted from the assumption of different thicknesses was $^{+1.6}_{-1.3}$ and $^{+3.1}_{-2.8}$ e^2 fm^4 for ^{21}Ne and ^{21}Na, respectively.

5. ^{48}Ti 2^+ *static electric quadrupole moment*

The effect of varying the static quadrupole moment of the first excited state of ^{48}Ti was examined by varying it between the upper and lower values of its uncertainty [29]. This resulted in variations of $^{+2.8}_{-1.0}$ and $^{+4.0}_{-1.4}$ e^2 fm^4 for ^{21}Ne and ^{21}Na, respectively. The effect of assuming quadrupole moments of zero and the matrix element from the simple quadrupole rotor model (0.321 e b) were also examined, resulting in variations of $^{+3.9}_{-1.4}$ and $^{+5.4}_{-2.0}$ e^2 fm^4 for ^{21}Ne and ^{21}Na, respectively, though it was decided that these were excessive owing to the existence of the more precise measurement [29].

6. ^{21}Ne, ^{21}Na $\frac{5}{2}^+$ *static electric quadrupole moment*

The static quadrupole moments of the first excited states in ^{21}Ne and ^{21}Na are unknown, and so the effect of varying these over a large range was examined. Values of zero and 0.2 e b (drastically larger than the shell-model-calculated values) were tested. The resulting variations in the $B(E2)\downarrow$ values were $^{+0.27}_{-0.05}$ and $^{+0.9}_{-0.2}$ e^2 fm^4 for ^{21}Ne and ^{21}Na, respectively.

7. ^{21}Ne, ^{21}Na $\frac{3}{2}^+ \rightarrow \frac{7}{2}^+$ $E2$ *matrix element*

The effect of varying the $E2$ matrix element of the competing excitation from the ground state was examined. In the case of ^{21}Ne, the upper and lower values of the adopted $B(E2)$ value were used, whereas for ^{21}Na, where the calculated $B(E2)$ used for the GOSIA calculations was higher than the upper range of the adopted value—16(8) W.u. [8]—only the lower value of this range was tested. The resulting uncertainty contributions were $^{+0.02}_{-0.01}$ and -0.66 e^2 fm^4 for ^{21}Ne and ^{21}Na, respectively.

8. *All other* ^{48}Ti *matrix elements*

Because of the weak dependence of the $2^+ \rightarrow 0^+$ yield on the remaining matrix elements in ^{48}Ti, all were varied in magnitude simultaneously in the same direction to investigate their effect. For those values for which a measured value was used in the GOSIA calculations, the upper and lower bounds of the quoted uncertainty range were used. For those transitions for which the simple quadrupole rotor model values were used, as discussed in Sec. III B, the matrix elements were varied by $\pm50\%$. Despite this coherent reduction or increase of several matrix elements simultaneously, the resulting contributions to the $B(E2)\downarrow$ uncertainties were only $^{+0.53}_{-0.36}$ and $^{+0.71}_{-0.36}$ e^2 fm^4 for ^{21}Ne and ^{21}Na, respectively.

9. *All other* ^{21}Ne, ^{21}Na *matrix elements*

Similarly, all other beam particle matrix elements were varied coherently in magnitude. Quoted uncertainties were used for transitions for which they were known, and a matrix element uncertainty of $\pm50\%$ was used for those values determined from shell-model calculations. The resulting uncertainty contributions to the $B(E2)\downarrow$ values were $^{+0.74}_{-0.21}$ and $^{+1.1}_{-0.4}$ e^2 fm^4 for ^{21}Ne and ^{21}Na, respectively.

10. *Corrections to the Rutherford orbit*

Four small effects change the Rutherford orbit, as discussed in Ref. [38]: dipole polarization, screening by atomic electrons, vacuum polarization, and relativistic correction of the nuclear masses. The first of these is corrected for in the GOSIA calculations, and the latter three have differing signs, leading to approximate cancellation. The effect of vacuum polarization changes the Coulomb interaction energy by $\sim0.5\%$ [39], though this effect is minimized by the projectile/target yield ratio method used in this analysis. The relativistic correction of the nuclear masses changes the scattering orbit, though with $v/c \simeq 0.06$ in this experiment, this leads to a small contribution of $\sim0.5\%$ [38]. An example of the effect of approximate cancellation of these effects can be found in Ref. [40] for ^{82}Se incident upon ^{48}Ti, based on formulas in Ref. [41]. The result is a correction magnitude less than 0.22%. To encompass the largest possible correction required for this experiment, an uncertainty contribution of 0.5% was assigned.

11. *Coulomb-nuclear interference and quantal corrections*

The choice of ^{21}Ne and ^{21}Na kinetic energy in this experiment was determined by the standard Coulomb barrier energy discussed in Ref. [42]. For ions lighter than ^{16}O, calculations using PTOLEMY [43] provide reliable estimates of the influence of Coulomb-nuclear interference, though for

heavier ions the satisfaction of the safe energy criterion results in a nuclear excitation interference of <0.1.

The applicability of the semiclassical approximation is determined by the magnitude of the Sommerfeld parameter η relative to I. For the nuclei in this experiment, $\eta = 27.1$ for ^{21}Ne and $\eta = 29.9$ for ^{21}Na, for $I = \frac{5}{2}$. The difference between quantum-mechanical analysis and semiclassical approximation results were examined in heavy-ion Coulomb excitation calculations [44], for which the effects are minimized by the projectile/target yield ratio method used in this analysis [45]. By extrapolating from a difference for low-spin excitation of 0.3%, and scaling by the ratio of the Sommerfeld parameters, the difference between the semiclassical results and a quantum-mechanical treatment for this experiment was taken to be 2.7% for ^{21}Ne and 2.5% for ^{21}Na.

C. $B(E2)$ values

Adding all of the uncertainty contributions in quadrature (using the larger magnitude when the upper and lower limits differed) yielded the following final results for ^{21}Ne: $B(E2)\downarrow = 87.5 \pm 5.8\, e^2$ fm^4, $B(E2)\uparrow = 131 \pm 9\, e^2$ fm^4, and $B(E2) = 25.4 \pm 1.7$ W.u. This has an uncertainty of 6.6% and is in excellent agreement with the previously accepted value of 24 ± 3 W.u. [8], although it is nearly twice as precise. Using the first $\frac{5}{2}^+$ state half-life from Ref. [8], 7.13 ± 0.14 ps, we obtain a mixing ratio of $\delta = (-)0.0767 \pm 0.0027$ and a $B(M1)$ value of $B(M1)\downarrow = 0.1274 \pm 0.0025\, \mu_N{}^2$, where

$$\delta = 0.835 E_\gamma\,(\text{MeV})\,\frac{\langle I_f||E2||I_i\rangle}{\langle I_f||M1||I_i\rangle}, \tag{4}$$

I_i is the initial state, and I_f is the final state, with phase as defined in Ref. [37].

For radioactive ^{21}Na, our results are $B(E2)\downarrow = 136.5 \pm 9.2\, e^2$ fm^4, $B(E2)\uparrow = 205 \pm 14\, e^2$ fm^4, and $B(E2) = 39.7 \pm 2.7$ W.u., which has an uncertainty of 6.7% and is significantly different and more precise than the previously adopted value of 14 ± 12 W.u. [8]. Using the first $\frac{5}{2}^+$ state half-life from Ref. [8], 7.08 ± 0.08 ps, we obtain a mixing ratio of $\delta = (+)0.0832 \pm 0.0028$ and a $B(M1)$ value of $B(M1)\downarrow = 0.1513 \pm 0.0017\, \mu_N{}^2$.

V. DISCUSSION

To examine whether the observed relationship between the $B(E2)$ values is present in calculations, ^{21}Ne and ^{21}Na have been examined in the framework of the nuclear shell model using both the *p-sd* [33,34] and USDB [46] effective interactions. All calculations were carried out with the OXBASH shell-model code [34]. Effective charges of $e_p = 1.5e$ and $e_n = 0.5e$ and free spin g factors quenched by 0.7 were used, in agreement with previous calculations in this region.

The *p-sd* shell-model calculation is based on $1p_{1/2}$ and *sd*-shell interactions, with an inert ^{12}C core [33,34]. For ^{21}Ne, transition strengths of $B(E2; \frac{5}{2}^+ \rightarrow \frac{3}{2}^+) = 30.7$ W.u. and $B(M1; \frac{5}{2}^+ \rightarrow \frac{3}{2}^+)\downarrow = 0.09\, \mu_N{}^2$ were calculated. For ^{21}Na, the values calculated were $B(E2; \frac{5}{2}^+ \rightarrow \frac{3}{2}^+) = 36.4$ W.u. and $B(M1; \frac{5}{2}^+ \rightarrow \frac{3}{2}^+)\downarrow = 0.11\, \mu_N{}^2$. These agree reasonably with the experimental $B(E2)$ values of 25.4 ± 1.7 and 39.7 ± 2.7 W.u., although the difference between the mirror pairs is somewhat larger in experiment than theory using these effective charges.

Similar results are obtained by using the recently derived USDB interaction [46] with ^{16}O as the inert core. For ^{21}Ne, transition strengths of $B(E2; \frac{5}{2}^+ \rightarrow \frac{3}{2}^+) = 30.9$ W.u. and $B(M1; \frac{5}{2}^+ \rightarrow \frac{3}{2}^+)\downarrow = 0.10\, \mu_N{}^2$ were calculated. For ^{21}Na, the values calculated were $B(E2; \frac{5}{2}^+ \rightarrow \frac{3}{2}^+) = 36.5$ W.u. and $B(M1; \frac{5}{2}^+ \rightarrow \frac{3}{2}^+)\downarrow = 0.11\, \mu_N{}^2$.

The calculations from both of these models agree well with each other and match the trends in the observed $B(\lambda L)$ values. The orbital occupancies calculated for the $\frac{3}{2}^+$ and $\frac{5}{2}^+$ states are similar, with the $T = \frac{1}{2}$ five $d_{5/2}$ nucleon states as the main configuration. The large $E2$ transition strengths observed here can be attributed to the similar wave functions between these states. The larger $B(E2)$ value for ^{21}Na is due to the larger number of protons. This can be seen by increasing the difference between the proton and neutron effective charges. Using $e_p = 1.7e$ and $e_n = 0.3e$, we obtain $E2$ strengths of 29.6 and 37.5 W.u. for ^{21}Ne and ^{21}Na, respectively, in somewhat better agreement with the experimental values, and demonstrating the degree of sensitivity of the calculations to the effective charges.

Examining these nuclei with regard to the collective model, the β_2 deformation parameter values can be determined by assuming the simple macroscopic prolate quadrupole rotor model as described by

$$\langle K, I_2\|E2\|K, I_1\rangle = \sqrt{(2I_1+1)}\langle I_1\, K\, 2\, 0\,|\, I_2\, K\rangle\sqrt{\frac{5}{16\pi}}eQ_0, \tag{5}$$

where Q_0 is the intrinsic quadrupole moment given by

$$Q_0 = \frac{3}{\sqrt{5\pi}}ZR^2\beta_2, \tag{6}$$

and with nuclear radii taken to be $R = 1.2\, A^{\frac{1}{3}}$ fm. The β_2 values for ^{21}Ne and ^{21}Na that result are 0.611 ± 0.020 and 0.693 ± 0.023, respectively. By using the adopted $B(E2)$ values of their first excited levels [47–49], the β_2 values of neighboring even-even nuclei are determined to be 0.714 ± 0.018 for ^{20}Ne, 0.560 ± 0.011 for ^{22}Ne, and 0.613 ± 0.014 for ^{24}Mg, with which the results of this analysis are consistent.

VI. CONCLUSIONS

The low-energy structures of ^{21}Ne and radioactive ^{21}Na have been studied by using Coulomb excitation to resolve a discrepancy in ^{21}Na between previously measured results and shell-model calculations and to provide precise structure information for this nucleus. The measured $B(E2)\uparrow$ values found are $131 \pm 9\, e^2$ fm^4 (25.4 ± 1.7 W.u.) for ^{21}Ne and $205 \pm 14\, e^2$ fm^4 (39.7 ± 2.7 W.u.) for ^{21}Na, in agreement with shell-model calculations, demonstrating the inaccuracy of the value determined previously from mixing ratio measurements [12]. Mixing ratios of $\delta = (-)0.0767 \pm 0.0027$ for ^{21}Ne and

$\delta = (+)0.0832 \pm 0.0028$ for ^{21}Na were determined, resulting in $B(M1)\downarrow$ values of $0.1274 \pm 0.0025\,\mu_N{}^2$ for ^{21}Ne and $0.1513 \pm 0.0017\,\mu_N{}^2$ for ^{21}Na, when combined with previous lifetime measurements [9]. The results demonstrate that shell-model calculations, with appropriate choices of the effective charges, can provide accurate structure information for this nucleus of relevance to the breakout from the hCNO cycle into the rp-process in explosive astrophysical environments. As the first experiment with TIGRESS, these results provide a favorable outlook for future experiments with accelerated radioactive ion beams and high-efficiency HPGe detectors at ISAC-II.

ACKNOWLEDGMENTS

This work has been partially supported by the Natural Sciences and Engineering Research Council of Canada and by the U.S. Department of Energy by Lawrence Livermore National Laboratory under Contract No. DE-AC52-07-NA27344. The authors would also like to acknowledge the support offered by the U.S. Department of Energy under Grant Nos. DE-FG52-06-NA26194 and DE-FG02-97-ER41042, the U.S. National Science Foundation, and the Engineering and Physical Sciences Research Council of the United Kingdom. TRIUMF is funded via a contribution agreement with the National Research Council of Canada.

[1] M. Wiescher and H. Schatz, Nucl. Phys. **A693**, 269 (2001).
[2] W. Bradfield-Smith *et al*., Nucl. Instrum. Methods A **425**, 1 (1999).
[3] W. Bradfield-Smith *et al*., Phys. Rev. C **59**, 3402 (1999).
[4] D. Groombridge *et al*., Nucl. Phys. **A688**, 472c (2001).
[5] J. Görres, M. Wiescher, and F.-K. Thielemann, Phys. Rev. C **51**, 392 (1995).
[6] J. M. D'Auria *et al*., Phys. Rev. C **69**, 065803 (2004).
[7] C. Ruiz *et al*., Phys. Rev. C **65**, 042801(R) (2002).
[8] R. B. Firestone, Nuclear Data Sheets **103**, 269 (2004), with Oct. 16, 2006, National Nuclear Data Center online errata.
[9] P. M. Rowe *et al*., J. Phys. G **4**, 431 (1978).
[10] A. Anttila and M. Bister, Phys. Lett. **B29**, 645 (1969).
[11] A. Anttila, M. Bister, and J. Keinonen, Z. Phys. A **274**, 227 (1975).
[12] J. G. Pronko, R. A. Lindgren, and D. A. Bromley, Nucl. Phys. **A140**, 465 (1970).
[13] R. G. Sextro, R. A. Gough, and J. Cerny, Phys. Rev. C **8**, 258 (1973).
[14] J. N. Orce (private communication).
[15] C. E. Svensson *et al*., Nucl. Instrum. Methods A **540**, 348 (2005).
[16] H. C. Scraggs *et al*., Nucl. Instrum. Methods A **543**, 431 (2005).
[17] C. E. Svensson *et al*., J. Phys. G: Nucl. Part. Phys. **31**, S1663 (2005).
[18] M. A. Schumaker *et al*., Nucl. Instrum. Methods A **570**, 437 (2007).
[19] M. A. Schumaker *et al*., Nucl. Instrum. Methods A **573**, 157 (2007).
[20] M. A. Schumaker and C. E. Svensson, Nucl. Instrum. Methods A **575**, 421 (2007).
[21] R. E. Laxdal, Nucl. Instrum. Methods B **204**, 400 (2003).
[22] C. E. Svensson *et al*., Nucl. Instrum. Methods B **204**, 660 (2003).
[23] J.-P. Martin, C. Mercier, N. Starinski, C. J. Pearson, and P.-A. Amaudruz, IEEE Trans. Nucl. Sci. **55**, 84 (2008).
[24] P. Bricault, M. Dombsky, A. Dowling, and M. Lane, Nucl. Instrum. Methods B **204**, 319 (2003).
[25] T. W. Burrows, Nucl. Data Sheets **107**, 1747 (2006).
[26] http://www.srim.org.
[27] T. Czosnyka, D. Cline, and C. Y. Wu, Bull. Am. Phys. Soc. **28**, 745 (1983).
[28] T. W. Ducas, M. S. Feld, L. W. Ryan, Jr., N. Skribanowitz, and A. Javan, Phys. Rev. A **5**, 1036 (1972).
[29] P. M. S. Lesser, D. Cline, P. Goode, and R. N. Horoshko, Nucl. Phys. **A190**, 597 (1972).
[30] F. A. Beck, T. Byrski, G. J. Costa, and J. P. Vivien, Phys. Rev. C **16**, 679 (1977).
[31] R. Ernst *et al*., Phys. Rev. C **62**, 024305 (2000); A. Pakou, Phys. Rev. C **64**, 069801 (2001).
[32] M. Ogura *et al*., Hyperfine Interactions **159**, 235 (2004).
[33] D. J. Millener (private communication, 1984); B. H. Wildenthal, Prog. Part. Nucl. Phys. **11**, 5 (1984).
[34] OXBASH for Windows, B. A. Brown, A. Etchegoyen, N. S. Godwin, W. D. M. Rae, W. A. Richter, W. E. Ormand, E. K. Warburton, J. S. Winfield, L. Zhao, and C. H. Zimmerman, MSU-NSCL Report No. 1289.
[35] K. Krane, Nucl. Instrum. Methods **98**, 205 (1972).
[36] S. Agostinelli *et al*., Nucl. Instrum. Methods A **506**, 250 (2003).
[37] K. Krane and R. Steffen, Phys. Rev. C **2**, 724 (1970).
[38] D. Cline, Annu. Rev. Nucl. Part. Sci. **36**, 683 (1986).
[39] L. L. Foldy and E. Eriksen, Phys. Rev. **95**, 1048 (1954).
[40] A. E. Kavka *et al*., Nucl. Phys. **A593**, 177 (1995).
[41] K. Alder and A. Winther, *Electromagnetic Excitation* (North-Holland, Amsterdam, 1975).
[42] D. Cline, H. S. Gertzman, H. E. Gove, P. M. S. Lesser, and J. J. Schwartz, Nucl. Phys. **A133**, 445 (1969).
[43] M. Rhoades-Brown, M. H. Macfarlane, and Steven C. Pieper, Phys. Rev. C **21**, 2417 (1980).
[44] L. D. Tolsma, Phys. Rev. C **20**, 592 (1979).
[45] J. Stachel *et al*., Nucl. Phys. **A133**, 445 (1969).
[46] B. A. Brown and W. A. Richter, Phys. Rev. C **74**, 034315 (2006).
[47] D. R. Tilley, C. Cheves, J. Kelley, and H. Weller, Nucl. Phys. **A636**, 249 (1998).
[48] R. B. Firestone, Nucl. Data Sheets **106**, 1 (2005).
[49] R. B. Firestone, Nucl. Data Sheets **108**, 2319 (2007), with Dec. 12, 2007, National Nuclear Data Cente online errata.